

Solution-processed polycrystalline copper tetrabenzoporphyrin thin-film transistors

Patrick B. Shea^a, Lisa R. Pattison^b, Manami Kawano^c, Charlene Chen^a, Jihua Chen^d,
Pierre Petroff^b, David C. Martin^d, Hiroko Yamada^c, Noboru Ono^c, Jerzy Kanicki^{a,*}

^a *Organic & Molecular Electronics Laboratory, Department of Electrical Engineering & Computer Science, The University of Michigan, Ann Arbor, MI 48109-2108, USA*

^b *Department of Materials Science and Engineering, The University of California, Santa Barbara, CA 93106, USA*

^c *Department of Chemistry in the Faculty of Science, Ehime University, Bunkyo-cho 2-5, Matsuyama 790-8577, Japan*

^d *Department of Materials Science and Engineering, The University of Michigan, Ann Arbor, MI 48109, USA*

Received 19 June 2006; received in revised form 2 January 2007; accepted 9 January 2007

Available online 7 March 2007

Abstract

The demonstration of organic thin-film field-effect transistors (OFETs) using a solution-processable form of the organometallic molecule copper tetrabenzoporphyrin (CuTBP) is reported. A soluble precursor was spun-cast into an amorphous, insulating thin-film, and thermally annealed at 165 °C for 30 min into a polycrystalline organic semiconductor. Absorbance spectroscopy displayed characteristics of porphyrin macrocycles. Microscopy reveals the formation of domains comprising aligned nanorod aggregates with dimensions of 55 nm wide, 300 nm long, and 100 nm tall on the gate insulator surface. OFETs demonstrated field-effect mobilities typically on the order of 0.1 cm²/V s, threshold voltages around 5 V, subthreshold slopes around 4 V/dec, and ON/OFF-current ratios near 10⁴.

© 2007 Elsevier B.V. All rights reserved.

Keywords: Metallotetrabenzoporphyrins; X-ray diffraction; Atomic force microscopy; Optical absorption; Organic field-effect transistors; Solution processing

1. Introduction

Porphyrins and phthalocyanines as a class of macrocycles are exhaustively studied across a broad array of technical fields, with particular interest in biochemistry paid to metalloporphyrins, such as Fe-substituted heme and Mg-substituted chlorophyll [1–3]. The wealth of studies on porphyrin macrocycles therefore has produced a well-founded understanding on the interactions between porphyrins and other agents, such as light [4] or molecules [5], and how to customize the basic porphyrin molecule [6], for uses, such as in organic thin-film transistors and sensors [7–11]. Development of inexpensive and high-performance organic semiconductors similar to the metalloporphyrins prevalent in biochemical systems, coupled with novel organic electronic devices, may eventually lead to new generations of bio-compatible electron-

ics for applications, such as chemical sensing or drug delivery [12,13].

Organic thin-film field-effect transistors (OFETs) utilizing vacuum-deposited copper phthalocyanine (CuPc) as the active channel material were reported as early as 1996 [14], and with consistent improvement have attained field-effect mobilities on the order of 1 cm²/V s with single-crystals deposited via vacuum evaporation [15]. Films and OFETs fabricated from various evaporated MPcs have shown wide variation in electrical performance [16,17]. Substrate temperature during MPc thin-film deposition was shown to affect OFET electrical performance, with the optimal substrate temperature varying for each MPc. Furthermore, MPc crystallinity varied widely depending on metallation, for the same processing conditions. Typically, vacuum-deposited CuPc demonstrates the highest electronic performance, and as previously noted, has shown μ_{FE} exceeding 1 cm²/V s in single crystal OFETs [15]. Bao et al. also observed in MPcs a transition from granular shaped crystallites to elongated needles at elevated substrate temperatures, which they correlated to an increase in field-effect mobility in some MPcs [16].

* Corresponding author. Tel.: +1 734 936 0972; fax: +1 734 615 2843.

E-mail address: kanicki@eecs.umich.edu (J. Kanicki).

While free-base phthalocyanine has rarely been reported as the active material in an OFET [16], it has been shown that the like-molecule free-base tetrabenzoporphyrin (TBP) can be processed from solution to attain desirable OFET electrical characteristics, such as polycrystallinity, low OFF-current, sharp subthreshold behavior, and moderate field-effect mobility [18,19]. The synthesis of solution-processable TBP has been described, and can be furthered to substitute various atoms in the core of the TBP molecule [20–22]. Recently it has been shown that metallotetrabenzoporphyrins (MTBPs), similar to MPCs, can be used to fabricate OFETs from solution using a precursor form of the MTBP. These films demonstrate high field-effect mobilities, but also high overall conductivity [23].

In this work, we report the use of copper tetrabenzoporphyrin (CuTBP) as the active material in an OFET. A soluble, copper porphyrin complex was synthesized [22] and spun-cast from solution to form amorphous, insulating thin-films. Upon thermal annealing, the precursor converts into a polycrystalline organic semiconductor. Results from X-ray diffraction, transmission electron microscopy, optical microscopy, atomic force microscopy, and optical absorbance are also reported.

2. Experimental

Synthesis of the precursor molecule tetrabicyclo[2,2,2]octadienporphyrin copper complex or copper tetrabicycloporphyrin (CuCP), has been described [20–22]. In this case, 100 mg (0.16 mmol) of H₂CP and excess of Cu(OAc)₂/MeOH were dissolved in 20.0 mL of CHCl₃ and stirred at room temperature for 1 h. The conversion to metal complex was monitored by UV–vis spectra. After the solvent was removed under reduced pressure, the residue was dissolved in CHCl₃ and water was added. The separated organic phase was dried over Na₂SO₄ and the solvent was removed under reduced pressure, followed by purification by Al₂O₃ column chromatography using CHCl₃ as an eluent. The resulting solid was recrystallized by using CHCl₃–MeOH to give the Cu complex in 95% yield.

Prior to precursor deposition, all substrates were washed with acetone and isopropyl alcohol, dried in N₂, exposed to UV/ozone for 20 min, and soaked in 200-proof ethanol for 20 min. For all results described here, CuCP powder was dissolved in chloroform (0.9 wt.%) in air, and deposited onto the target substrate in the N₂ atmosphere of a glovebox. All solution depositions were followed by thermal annealing at 165 °C for 30 min in vacuum. Spun-cast films were on the order of 100 nm thick.

Atomic force microscopy (AFM) substrates were n⁺⁺ crystalline silicon (c-Si) coated with a 100 nm-thick thermal SiO₂ layer. AFM was performed in air using a Digital Instruments Multi-Mode NanoScope in tapping mode.

Electron microscopy samples were prepared by drop-casting diluted CuCP precursor solution onto copper grids, followed by thin-film conversion to CuTBP, and sandwiching to an amorphous carbon substrate. Samples were then analyzed using a Philips CM-12 scanning transmission electron microscope for crystallography and imaging.

For X-ray diffraction (XRD), the substrates were bare c-Si (n-type, 100 Ω cm, (1 0 0)). Powder-mode XRD in reflection

geometry was performed with a Philips XPERT MPD diffractometer with Cu Kα radiation (40 kV/30 mA) over 4° < 2θ < 35°. Thin-films analyzed using XRD were prepared by the previously discussed method. Powder CuCP and CuTBP samples were prepared for XRD by dispersing the powder across c-Si substrates using acetone, and heating the sample in situ. Crystallographic data (excluding structure factors) for the structure reported in this paper have been deposited with the Cambridge Crystallographic Data Centre as supplementary publication no. CCDC-609047. Copies of the data can be obtained free of charge via www.ccdc.cam.ac.uk/conts/retrieving.html or on application to The Director, CCDC, 12 Union Road, Cambridge CB2 1EZ, UK; fax: +44 1223 336 033; e-mail: deposit@ccdc.cam.ac.uk.

Quartz substrates and a Varian-Cary 500e UV–visible (UV–vis) spectrophotometer were used for obtaining optical absorbance spectra of precursor and thermally annealed thin-films. Absorbance versus photon energy ($h\nu$) was measured over a range of 1 ≤ $h\nu$ (eV) ≤ 6 in air at room temperature. For precursor films, the sample was baked at 90 °C in vacuum for 5 min to desolvate the thin-film but not convert the precursor. Following UV–vis measurements on the precursor thin-film, the same sample was then thermally annealed and fully converted by baking at 165 °C in vacuum. Following thermal conversion the absorbance spectrum was again measured.

Fourier transform infrared (FT-IR) spectroscopy [24] was performed using a Bio-Rad FTS-40 spectrometer. Undoped, double-side polished crystalline silicon (c-Si) substrates were used, and films formed by drop-casting precursor solutions onto the substrates; precursor films were desolvated by baking in vacuum for 5 min at 90 °C. The infrared absorbance of the precursor film was measured, followed by thermal annealing at 165 °C in vacuum for 30 min. The measurement was then repeated for the resulting thermally converted film. Absorbance versus wavenumber was measured at room temperature from 450 to 4000 cm⁻¹.

Substrates were n⁺⁺ crystalline silicon (c-Si) coated with a 100 nm-thick thermal SiO₂ layer. Following thermal annealing, OFET samples were completed by thermally evaporating Au (≈60 nm) through a stencil mask to form staggered source and drain (S/D) electrodes [25]. OFETs were measured in air and in the dark using a Hewlett-Packard 4156A semiconductor parameter analyzer, with contact to the gate electrode (n⁺⁺ c-Si) made using indium–gallium eutectic.

3. Results and discussion

3.1. Thin-film thermal conversion and infrared spectroscopy

The precursor molecule, tetrabicyclo[2,2,2]octadienporphyrin copper complex or copper tetrabicycloporphyrin (CuCP), was synthesized using the previously described method [20–22]. Upon thermal annealing, in this case at 165 °C for 30 min, the tetrabicyclo units each lose an ethylene molecule (C₂H₄) to form the tetrabenzoporphyrin copper complex (CuTBP). The precursor and semiconducting CuCP and CuTBP molecules, respectively, are shown in Fig. 1.

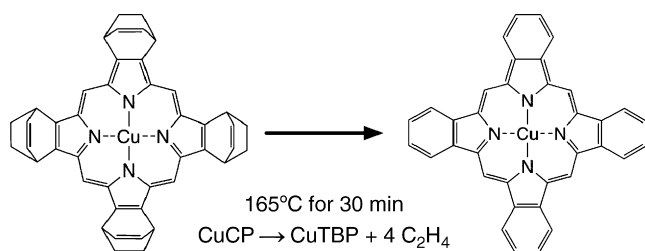


Fig. 1. Thermal conversion of CuCP to CuTBP.

Fourier transform infrared (FT-IR) and UV–vis spectroscopy are two optical methods that can be used to follow the conversion of the CuCP precursor to the CuTBP semiconductor. The FT-IR absorption spectra of copper-substituted macrocycles from literature typically display similar characteristics, and assignments have been made to most of the experimentally observed absorbance peaks [26–32]. Metallation of porphine has typically been noted to produce far-IR absorption peaks below 600 cm^{-1} , with the N–M stretching band (ν) in particular assigned to absorption peaks between 400 and 200 cm^{-1} [26,27]. Ogoshi et al., for example, observed and made vibrational assignments for IR absorbance peaks resulting from ν stretching of CC and CN, δ bending of CH, and π out-of-plane bending of CH and the porphine ring as summarized in Table 1 [26]. Furthermore, benzene exhibits IR absorbance peaks at $670, 770, 840, 1033,$ and 1170 cm^{-1} either of stronger intensity than, or not observed in, ethylene [33].

FT-IR absorption spectra for CuCP and CuTBP films between 3500 and 450 cm^{-1} are shown in Fig. 2. CuTBP in comparison to CuCP reveals increased IR absorbance in the peak at 627 cm^{-1} ; broadening of the peak at 791 cm^{-1} into a shoulder; the formation of a doublet peak at 837 cm^{-1} ; the appearance of a peak at 970 cm^{-1} ; and the appearance of a doublet peak at 1109 cm^{-1} . We focus on these peaks as potentially indicating the conversion from CuCP to CuTBP as they lie near the IR absorbance peaks of pure benzene, especially at 837 and 847 cm^{-1} . Furthermore, CuCP displays the strong band of IR absorbance peaks near 3000 cm^{-1} also observed in gaseous porphyrins [30] whereas after thermal annealing and crystallization the intensities of these bands decrease significantly. The previously mentioned vibrational assignments for the IR absorbance peaks in copper porphyrins lie close to the IR absorbance peaks observed in Fig. 2, indicating that equivalent or similar assignments can be made for solid CuCP and CuTBP [26–31]. A summary of the previous assignments for copper porphine, as

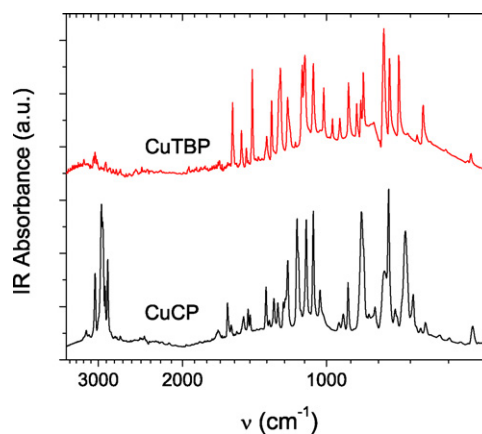


Fig. 2. Infrared absorbance spectra for solid CuCP and CuTBP on c-Si.

well as the experimentally measured peaks in solid CuTBP, are given in Table 1.

3.2. X-ray diffraction

X-ray diffraction (XRD) spectra for drop-cast films of CuCP and thermally annealed CuTBP, as well as a powder sample of CuTBP, are shown in Fig. 3a. The background has been removed from the drop-cast spectra to enhance viewing of the diffraction peaks. Drop-cast CuCP thin-films display an XRD spectrum typical of an amorphous film, with no discernible diffraction peaks indicative of significant crystal plane formation. Following thermal annealing at 165°C for 30 min and conversion, CuTBP displays significant diffraction peaks, indicating the formation of crystal planes. Drop-cast CuTBP films display the same diffraction peaks positions as CuTBP powder thermally converted at 165°C from CuCP powder, indicating that powder and solution-processed CuTBP have the same crystal structure. The 2θ positions of the diffraction peaks of CuTBP are similar to those of TBP and NiTBP [20,23] indicating that the three unit cells most likely have nearly iso-morphous crystallographic structures. It is also important to note here that TBP and NiTBP display variable morphological properties depending on thin-film surface coverage density. TBP display fractal aggregate growth in sparse films, and ordered aggregation in more densely covered films [19,34], while NiTBP aggregates display variable rod orientation with respect to their distance from the substrate surface, as well as large rod crystallization from precursor films, before thermal conversion to NiTBP [23]. CuTBP, on the other

Table 1
Comparison of IR absorbance in Cu-porphine (CuP) [26,32] and solid CuCP and CuTBP

Assignment [26,32]	CuP (cm^{-1}) [26,32]	CuCP (cm^{-1})	CuTBP (cm^{-1})
π (ring)	512, 702, 745, 900	494, 741, 901	498, 706, 737, 899
π (CH)	848, 861	845	847, 864
δ (CCN)	698, 1057, 1450	1065, 1443	706, 1065, 1430
δ (CH)	1057, 1151, 1310, 1387	1065, 1152, 1318	1065, 1161, 1302, 1387
ν (CC)	998, 1057, 1387, 1534, 1567, 1655, 1715	1065, 1540, 1582	1013, 1065, 1387, 1507, 1570, 1653, 1675
ν (CN)	998, 1057, 1450, 1534, 1655	1065, 1443, 1540	1013, 1065, 1430, 1507, 1653
ν (CH)	3025, 3120	3046, 3179	3048, 3067

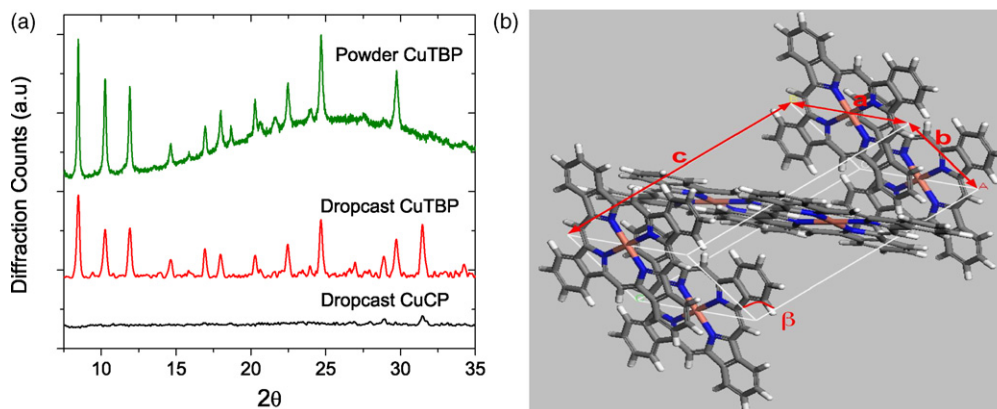


Fig. 3. (a) X-ray diffraction spectra for drop-cast CuCP and CuTBP, and powder CuTBP, and (b) the proposed unit cell structure of solid CuTBP.

hand, display no such morphological variations, such that the crystallographic properties of drop-cast and spun-cast thin-films were identical. Thicker drop-cast films were used to obtain the XRD spectra in Fig. 3a, but are also representative of the crystallographic properties of the spun-cast thin-films used for OFET measurements. The drop-cast spectra are shown in Fig. 3a for their better signal-to-noise characteristics.

Based on the XRD spectra of both powder and drop-cast CuTBP shown in Fig. 3a, the CuTBP unit cell was determined by a combination of powder diffraction refinement methods to fit the experimental XRD data ($R_{wp} < 3\%$, representing the difference between the experimental XRD spectrum and the simulated XRD spectrum of the fitted unit cell) and minimize the unit cell potential energy [35–38]. The unit cell (Fig. 3b) was found to be monoclinic with $P2_1/n$ symmetry, with lattice constants of $a = 1.239$ nm, $b = 0.6585$ nm, $c = 1.515$ nm, and $\beta = 101.16^\circ$, and a volume of 1212.4 \AA^3 .

3.3. Atomic force and transmission electron microscopy

As expected from XRD analysis, atomic force microscopy (AFM) height micrographs of spun-cast CuCP in Fig. 4a indicates the films are amorphous and smooth; dark spots indicate pits in the film. AFM micrographs of CuTBP following thermal conversion at 165°C for 30 min are shown in Fig. 4b–c. During thermal annealing CuCP converts into CuTBP nanorod-shaped crystallites having dimensions on the order of 55 nm

wide, 300 nm long, and 100 nm tall. In very thin or sparse thin-films (Fig. 4b), CuTBP nanorods tend to lie on the substrate with no mass orientation. In thicker films (Fig. 4c), CuTBP nanorods form domains where the individual nanorods are aligned parallel to each other, with the nanorod domains exceeding $10 \mu\text{m}$ in diameter. Furthermore, as evidenced by the relatively uniform height in Fig. 4c, the CuTBP nanorods display a tendency to lay similarly on the gate insulator surface, rather than piling randomly atop each other. In Fig. 4c, the edge of a nanorod domain is readily observed by the change in nanorod aggregation direction, as indicated by the dashed white lines. Furthermore, whereas NiTBP displayed variation in nanorod growth orientation away with distance from the dielectric surface [23], very thin spun-cast films of CuTBP display the same nanorod aggregation tendency as the continuous and thicker spun-cast films shown in Fig. 4c.

Transmission electron microscopy (TEM) micrographs of CuCP and CuTBP thermally annealed at 165°C for 30 min are shown in Fig. 5, and were used to further examine the submicrometer-scale properties of polycrystalline CuTBP. TEM micrographs of CuCP (Fig. 5a) appear amorphous, and display no discernible diffraction patterns. After vacuum thermal annealing at 165°C for 30 min, CuTBP nanorods are clearly observed. In CuTBP samples (Fig. 5b) where nanorod surface coverage density is sparse, rod orientation is random. In many cases, however, rings of CuTBP aggregates of unknown origin are observed, with varying radii. In samples with increased

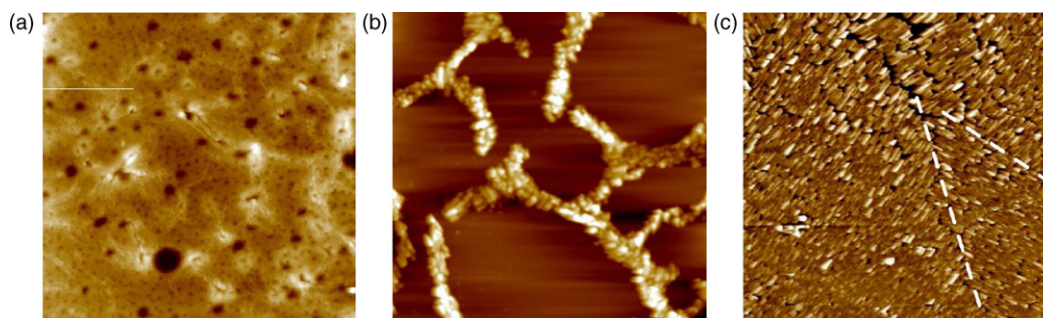


Fig. 4. AFM height micrographs of (a) CuCP and (b–c) CuTBP thin-films spun-cast onto SiO_2 . Axes dimensions and height scale in (a and c) are $10 \mu\text{m} \times 10 \mu\text{m}$ and 100 nm, respectively, and in (b) $5 \mu\text{m} \times 5 \mu\text{m}$ and 150 nm, respectively. The dashed lines in (c) indicate boundaries where nanorod direction changes.

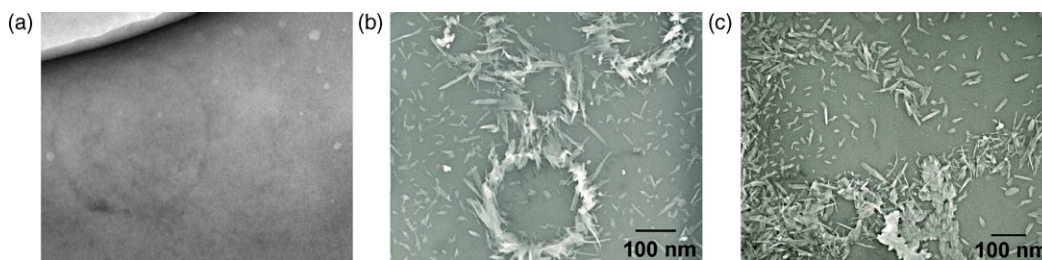


Fig. 5. TEM micrographs of: (a) precursor CuCP, (b) sparse CuTBP, and (c) more dense CuTBP with parallel aggregation, drop-cast onto Cu grids coated with amorphous carbon.

CuTBP nanorod surface coverage density (Fig. 5c), the same parallel nanorod orientation seen in CuTBP AFM micrographs with higher surface coverage density (Fig. 4c) is observed.

AFM and TEM measurements reveal similar submicrometer-scale aggregation of CuTBP nanorods. Aggregation of porphyrins in solution or in solid form have been widely studied due to the prevalence of aggregated porphyrins in important biological systems, such as chlorophyll [39–43]. In such porphyrins aggregation tends to occur in either the J-aggregate (edge-to-edge) or H-aggregate (face-to-face) formation [44]. Aggregation in water-soluble Cu(II) tetraphenylporphyrins, for example, showed that aggregation order and rate in solution depended upon solution concentration and charge type on the molecule's periphery [40], or the addition dimethylformamide or dimethyl sulphoxide to the solution [39]. In these cases, aggregation was a process of polymerization of the porphyrin monomer in solution, with the order of the aggregates varying widely. AFM imaging of several protonated tetraphenylporphyrins (TPPs) on glass revealed similar J-aggregate formations as observed here, although without micrometer-scale alignment [45]. The results shown here represent the thermal conversion of an amorphous precursor molecule into a symmetric crystallographic unit cell, rather than polymerization of a CuTBP molecule. In the case of precursor-deposited CuTBP, aggregation and domain formation, as previously noted, depend on the surface coverage of the spun-cast film; nanorod shape, on the other hand, is consistent.

3.4. Optical absorption and microscopy

Due to the insoluble nature of the simple porphyrin molecule, most reports of the optical properties of tetrabenzoporphyrins have involved single molecules in the gaseous phase or suspended in solution [1]. Porphyrins typically display absorption spectra [46] with a strong absorption band in the near-UV range around photon energies ($h\nu$) of 3 eV (the Soret, or B, band). Weaker absorption bands in the visible range between $1.75 < h\nu$ (eV) < 2.75 (Q bands) also appear, with peak multiplicity and energy positions related to peripheral and core substituents. Solid metal-free TBP deposited via solution from a precursor form displayed the previously mentioned traits [19,47], as did solid NiTBP [23].

Optical absorbance spectra for solid, spun-cast CuCP and CuTBP thin-films on quartz substrates are shown in Fig. 6. Similar absorbance spectra were obtained for drop-cast CuCP and

CuTBP films, indicating similar electronic transitions, but are not included here. The two spectra shown here were taken for the same film before and after vacuum thermal annealing at 165 °C for 30 min. The absorbance maximum for CuTBP occurs at a photon energy of 2.8 eV, with additional peaks at 1.9, 2.1, 3.9, and 5.1 eV. The absorbance maximum for CuCP occurs at a photon energy of 3.1 eV, with additional peaks at 2.2, 2.4, 3.6, and 5.1 eV. The absorption peaks in CuCP for $h\nu < 3$ eV red-shift by approximately 0.3 eV, while the peak at 5.1 eV retains its position. Similar absorption spectra were found for free-base and copper phthalocyanine [46], in which the Soret band was assigned to an optical transition at 3.7 eV. Additionally, the absorption spectra of free-base and Cu-substituted phthalocyanine are similar [46], as is observed here for solid CuTBP compared to metal-free TBP. Furthermore, the four-fold symmetry of CuCP and CuTBP produces two absorption peaks in the Q band in Fig. 6 (around 1.9 eV), whereas CP and TBP have two-fold symmetry and displayed four absorption peaks in the Q band [47].

It has been proposed that the limiting factors in electronic devices fabricated from polycrystalline organic semiconductors, such as pentacene are the crystalline grain size and the grain boundary density [48,49]. The polarized optical micrograph in Fig. 7 displays, on a larger scale, the polycrystalline nature of the CuTBP thin-films. The electrodes seen in the micrograph are 20 μm wide, indicating that CuTBP forms into crystalline domains of approximately the same size, wherein the previously described nanorods are aligned parallel to each other. Furthermore, the domains appear to have no preferred shape

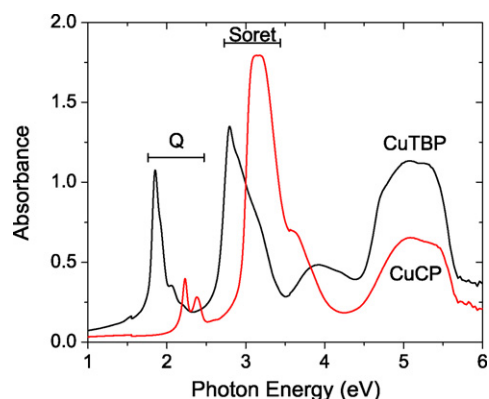


Fig. 6. Optical absorbance spectra for spun-cast CuCP and CuTBP thin-films on quartz.

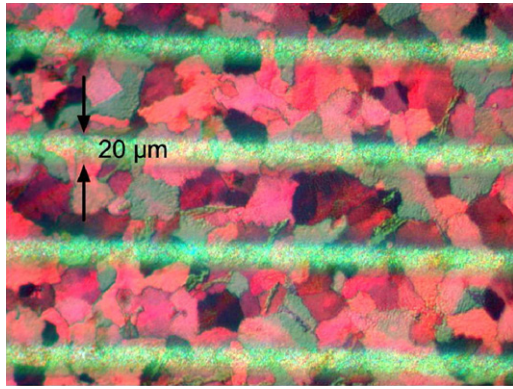


Fig. 7. Polarized optical micrograph of a continuous, spun-cast CuTBP thin-film on thermally oxidized c-Si. The electrodes shown in the figure are 20 μm wide. Color variations in the film indicate individual nanorod domains. (For interpretation of the references to color in this figure legend, the reader is referred to the web version of the article.)

or direction. By comparison, NiTBP forms crystals approaching 1 mm in diameter [23] and TBP on the order of 2 μm in diameter [19].

3.5. Thin-film transistors

The electrical measurements presented here are for a single device with a channel width (W) of 1040 μm and channel length (L) of 32.5 μm. Spun-cast films used for OFETs were typically on the order of 100 nm thick, as confirmed by AFM measurements. CuTBP OFET output (drain current, I_D , versus drain–source bias, V_{DS}) characteristics are shown in Fig. 8. At low V_{DS} , increasing the gate–source bias, V_{GS} , beyond –20 V has little effect on I_D . Furthermore, a nonlinear dependence with V_{DS} at low drain bias is apparent, both effects indicating the presence of large source and drain contact resistances possibly associated with the formation of non-ohmic source and drain electrodes.

CuTBP OFET transfer (I_D versus V_{GS}) characteristics are shown in Fig. 9a and b, on linear and semi-log scales, respectively. Also in Fig. 9b, an OFF-current of –3 nA is observed at $V_{GS} = 20$ V, indicating an ON-/OFF-current ratio of nearly 10^4 if the ON-current is taken at $V_{GS} = -40$ V. However, I_D saturates at more negative V_{GS} , similar to the nonlinear I_D behavior observed

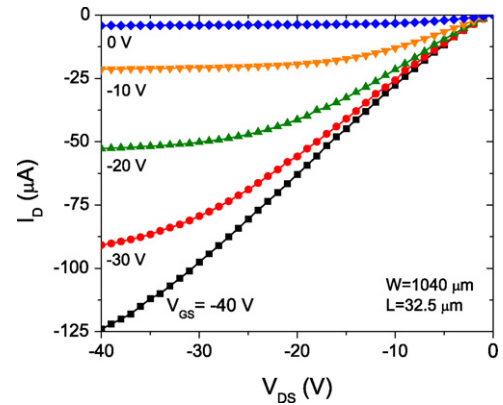


Fig. 8. Output characteristics of a CuTBP OFET.

in Fig. 8. This behavior possibly results from non-ohmic source and drain electrodes, such that a Schottky barrier limits charge injection and extraction at more negative V_{GS} [50]. Whereas in c-Si metal-oxide-semiconductors field-effect transistors (MOSFETs) electrical parameters, such as the inversion threshold voltage, V_T , can be accurately calculated based on known material parameters, in OFETs the typical current–voltage relations for MOSFETs are used to extract OFET electrical parameters, such as the extracted field-effect mobility (μ_{FE}) and the extracted accumulation threshold voltage (V_T). The gradual-channel approximation of the current–voltage relations can be described by [50]

$$I_D^{Lin} = -\frac{W}{L} \mu_{FE}^{Lin} C_i (V_{GS} - V_T^{Lin}) V_{DS} \quad (1)$$

in the linear regime ($|V_{DS}| < |V_{GS} - V_T|$), and by

$$I_D^{Sat} = -\frac{W}{2L} \mu_{FE}^{Sat} C_i (V_{GS} - V_T^{Sat})^2 \quad (2)$$

in the saturation regime ($|V_{DS}| > |V_{GS} - V_T|$). The values for μ_{FE} and V_T , as described in Eqs. (1) and (2) were determined by using a straight-line fit (shown by solid lines in Fig. 9a) of the CuTBP OFET electrical data to Eq. (1) and the square-root of Eq. (2). Using this simple straight-line approximation, in the linear regime ($V_{DS} = -5$ V) we find $\mu_{FE} = 0.1$ cm²/V s and $V_T = 5$ V; in the saturation regime ($V_{DS} = -60$ V), we find $\mu_{FE} = 0.13$ cm²/V s and $V_T = 7.5$ V. No channel length depen-

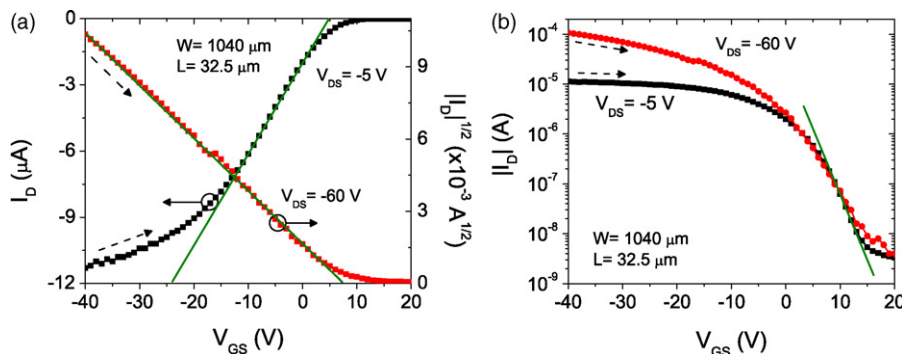


Fig. 9. Transfer characteristics of a CuTBP OFET. Dashed arrows indicate the measurement direction. In (a), the solid lines indicate the fits to Eqs. (1) and (2); in (b), the solid line indicates calculation of the subthreshold slope.

dence of μ_{FE} and V_T was observed. From Fig. 9b, a subthreshold slope of 4.2 V/dec was extracted for both the linear and saturation regimes. Extracted parameters such as μ_{FE} were observed to vary by approximately $\pm 33\%$ for CuTBP OFETs within the same substrate. Variation of the extracted μ_{FE} across different samples with the same properties (e.g., gate capacitance, electrode type and thickness) was as high as one order of magnitude from the results presented here in Figs. 8 and 9. This variation was observed typically to result from surface coverage density, such that samples with poor or sparse surface coverage density had non-continuous crystallization. It is also worth noting that continued exposure of the CuTBP OFETs to air leads to increased film conductivity, producing extracted field-effect mobilities exceeding $1 \text{ cm}^2/\text{V s}$, decreased ON-/OFF-current ratios around 10^2 , increased subthreshold slopes, and more positive (or less negative) V_T . The effects of air exposure were removed by thermal annealing in vacuum at 200°C , as also noted for phthalocyanine films [51].

The electrical performance of CuTBP OFETs is similar to that of NiTBP with respect to μ_{FE} and I_{OFF} [23]. The subthreshold slope of CuTBP is lower than for NiTBP, potentially resulting from the micrometer-scale alignment of the CuTBP aggregates (Fig. 4c), whereas NiTBP OFET films were reported to be composed of large, micrometer-scale needle-shaped aggregates lacking large-scale orientation, thus likely increasing the density of grain boundary interface trap states. With respect to TBP, CuTBP displays a μ_{FE} approximately two orders of magnitude higher [18,47], but also an I_{OFF} two orders of magnitude higher. The subthreshold slope in TBP OFETs was significantly lower than for CuTBP, indicating a higher density of trap states, possibly resulting from the larger, tightly packed (but not as ordered and symmetric) aggregates observed in TBP. Comparatively, the electrical performance of solution-processed CuTBP OFETs is in the same range as CuPc OFETs with a vacuum-deposited semiconductor layer, although the highest reported μ_{FE} values for CuPc in the order of $100 \text{ cm}^2/\text{V s}$ are attained without ambient exposure. The reported μ_{FE} varies similarly in a range of 10^{-2} – $100 \text{ cm}^2/\text{V s}$ [14–16], with OFF-currents between 10^{-10} and 10^{-9} A.

4. Conclusions

Polycrystalline, semiconducting thin-films of copper tetrabenzoporphyrin (CuTBP) were produced from amorphous, insulating thin-films of copper tetrabicycloporphyrin (CuCP) by thermal conversion of the precursor film at 165°C in vacuum. X-ray diffraction displayed no diffraction peaks for CuCP, but upon thermal conversion CuTBP displays numerous diffraction peaks indicative of crystal plane formation. Optical and IR absorbance displayed spectra characteristic of porphyrin macrocycles. Atomic force microscopy and transmission electron microscopy also displayed amorphous CuCP films converting into polycrystalline CuTBP, specifically revealing the formation of CuTBP nanorods. Thin-film transistors fabricated using polycrystalline CuTBP thin-films displayed field-effect mobilities on the order of $0.1 \text{ cm}^2/\text{V s}$, with accumulation threshold voltages around +5 V, subthreshold slopes of 4.2 V/dec, and ON-/OFF-

current ratios of approximately 10^4 . Solution-processed CuTBP OFET performance in terms of conductivity was similar to that of solution-processed NiTBP and vacuum-deposited CuPc, and two orders of magnitude higher than for solution-processed TBP.

References

- [1] K.M. Kadish, K.M. Smith, R. Guilard (Eds.), *The Porphyrin Handbook*, Academic Press, 1999.
- [2] K.M. Smith, Syntheses and chemistry of porphyrins, *J. Porphyrins Phthalocyanines* 4 (2000) 319–324.
- [3] A.D. Procyk, D.F. Bocian, Vibrational characteristics of tetrapyrrolic macrocycles, *Annu. Rev. Phys. Chem.* 43 (1992) 465–496.
- [4] H. Imahori, Giant multiporphyrin arrays as artificial light-harvesting antennas, *J. Phys. Chem. B* 108 (2004) 6130–6143.
- [5] D.B. Papkovsky, G.V. Ponomarev, W. Trettnak, P. O'Leary, Phosphorescent complexes of porphyrin ketones: optical properties and application to oxygen sensing, *Anal. Chem.* 67 (1995) 4112–4117.
- [6] R. Guilard, K.M. Kadish, Some aspects of organometallic chemistry in metalloporphyrin chemistry: synthesis, chemical reactivity, and electrochemical behavior of porphyrins with metal–carbon bonds, *Chem. Rev.* 88 (1988) 1121–1146.
- [7] A.R. Brown, C.P. Jarrett, D.M. de Leeuw, M. Matters, Field-effect transistors made from solution-processed organic semiconductors, *Synth. Met.* 88 (1997) 37–55.
- [8] G. Horowitz, Organic field-effect transistors, *Adv. Mater.* 10 (1998) 365–377.
- [9] S. Scheinert, G. Paasch, Fabrication and analysis of polymer field-effect transistors, *Phys. Status Solidi A* 201 (2004) 1263–1301.
- [10] H. Sirringhaus, Device physics of solution-processed organic field-effect transistors, *Adv. Mater.* 17 (20) (2005) 2411–2425.
- [11] M.K. Chan, Heme protein biosensors, *J. Porphyrins Phthalocyanines* 4 (2000) 358–361.
- [12] J.M. Shaw, P.F. Seidler, Organic electronics: introduction, *IBM J. Res. Dev.* 45 (1) (2001) 3–8.
- [13] J.M.J. Frechet, Functional polymers: from plastic electronics to polymer-assisted therapeutics, *Prog. Polym. Sci.* 30 (2005) 844–857.
- [14] Z. Bao, A.J. Lovinger, A. Dodabalapur, Organic field-effect transistors with high mobility based on copper phthalocyanine, *Appl. Phys. Lett.* 69 (20) (1996) 3066–3068.
- [15] R. Zeis, T. Siegrist, C. Kloc, Single-crystal field-effect transistors based on copper phthalocyanine, *Appl. Phys. Lett.* 86 (2005) 022103.
- [16] Z. Bao, A.J. Lovinger, A. Dodabalapur, Highly ordered vacuum-deposited thin films of metallophthalocyanines and their applications in field-effect transistors, *Adv. Mater.* 9 (1997) 42–44.
- [17] R.W.I. de Boer, A.F. Stassen, M.F. Craciun, C.L. Mulder, A. Molinari, S. Rogge, A.F. Morpurgo, Ambipolar Cu- and Fe-phthalocyanine single-crystal field-effect transistors, *Appl. Phys. Lett.* 86 (2005) 262109.
- [18] S. Aramaki, Y. Sakai, N. Ono, Solution-processible organic semiconductor for transistor applications: tetrabenzoporphyrin, *Appl. Phys. Lett.* 84 (2004) 2085–2087.
- [19] S. Aramaki, Y. Sakai, R. Yoshiyama, K. Sugiyama, N. Ono, J. Mizuguchi, Tetrabenzoporphyrin semiconductor for transistor applications, *Proc. SPIE* 5522 (2004) 27–35.
- [20] S. Ito, T. Murashima, H. Uno, N. Ono, A new synthesis of benzoporphyrins using 4,7-dihydro-4,7-ethano-2h-isoindole as a synthon of isoindole, *Chem. Commun.* (1998) 1661–1662.
- [21] S. Ito, N. Ochi, T. Murashima, H. Uno, N. Ono, A new synthesis of benzoporphyrins using 4,7-dihydro-4,7-ethano-2h-isoindole as an isoindole equivalent, *Heterocycles* 52 (2000) 399–411.
- [22] Y. Shimizu, Z. Shen, T. Okujima, H. Uno, N. Ono, First synthesis of a series of core-modified tetrabenzoporphyrins, *Chem. Commun.* (2004) 374–375.
- [23] P.B. Shea, L.R. Pattison, M. Kawano, J. Kanicki, P. Petroff, H. Yamada, N. Ono, Solution-processed nickel tetrabenzoporphyrin thin-films and field-effect transistors, *J. Appl. Phys.* (2006) 034502.

- [24] P.R. Griffiths, J.A. De Haseth, *Fourier Transform Infrared Spectrometry*, second ed., Wiley-Interscience, 1986.
- [25] R. Street, A. Salleo, Contact effects in polymer transistors, *Appl. Phys. Lett.* 81 (2002) 2887–2889.
- [26] H. Ogoshi, Y. Saito, K. Nakamoto, Infrared spectra and normal coordinate analysis of metalloporphyrins, *J. Chem. Phys.* 57 (1972) 4194–4202.
- [27] L.L. Gladkov, K.N. Solovyov, The normal coordinate analysis of porphyrin and its derivatives based on the solution of the inverse spectral problem for porphyrin and Cu porphyrin. II. A valence force field for in-plane vibrations of the Cu porphyrin molecule, *Spectrochim. Acta, Part A* 41 (1985) 1443–1448.
- [28] S. Hu, T.G. Spiro, The origin of infrared marker bands of porphyrin π -cation radicals: infrared assignments of cations of copper(II) complexes of octaethylporphine and tetraphenylporphine, *J. Am. Chem. Soc.* 115 (1993) 12029–12034.
- [29] J.R. Kincaid, M.W. Urban, T. Watanabe, K. Nakamoto, Infrared spectra of matrix-isolated metal complexes of octaethylporphine, *J. Phys. Chem.* 87 (1983) 3096–3101.
- [30] C.J. Pouchart, *The Aldrich Library of FT-IR Spectra*, vol. 3, second ed., Aldrich, 1997.
- [31] M.K. Debe, Extracting physical structure information from thin organic films with reflection absorption infrared spectroscopy, *J. Appl. Phys.* 55 (1984) 3354–3366.
- [32] L.J. Boucher, J.J. Katz, The infrared spectra of metalloporphyrins ($4000\text{--}160\text{ cm}^{-1}$), *J. Am. Chem. Soc.* 89 (1967) 1340–1345.
- [33] NIST Chemistry WebBook, <http://webbook.nist.gov/chemistry/>.
- [34] L.K. Pattison, Structural characterizations of organic semiconductor thin-films, Ph.D. Thesis, University of California, Santa Barbara, 2006.
- [35] G.S. Pawley, Unit-cell refinement from powder diffraction scans, *J. Appl. Cryst.* 14 (1981) 357–361.
- [36] R.A. Young, *The Rietveld Method*, IUCr Monographies of Crystallography, vol. 5, Oxford University Press, 1993.
- [37] G.E. Engel, S. Wilke, K.D.M. Harris, F.J.J. Leusen, PowderSolve—a complete package for crystal structure solution from powder diffraction patterns, *J. Appl. Cryst.* 32 (1999) 1169–1179.
- [38] D.A. Van Veldhuizen, G.B. Lamont, Multiobjective evolutionary algorithms: analyzing the state-of-the-art, *Evol. Comput.* 8 (2000) 125–147.
- [39] J.A. De Bolfo, T.D. Smith, J.F. Boas, J.R. Pilbrow, An electron spin resonance study of the aggregation of copper(II) water-soluble porphyrins, *J.C.S. Dalton* (1975) 1523–1525.
- [40] R.F. Pasternack, L. Francesone, D. Raff, E. Spiro, Aggregation of nickel(II), copper(II), and zinc(II) derivatives of water-soluble porphyrins, *Inorg. Chem.* 12 (1973) 2606–2611.
- [41] S.H. Eichhorn, D.W. Bruce, D. Guillon, J.-L. Gallani, T. Fischer, J. Stumpe, T. Geue, Metal ion mediated mesomorphism and thin film behaviour of amphitropic tetraazoporphyrin complexes, *J. Mater. Chem.* 11 (2001) 1576–1584.
- [42] D.L. Akins, H.-R. Zhu, C. Guo, Aggregation of tetraaryl-substituted porphyrins in homogeneous solution, *J. Phys. Chem.* 100 (1996) 5420–5425.
- [43] M. Kawao, H. Ozawa, H. Tanaka, T. Ogawa, Synthesis and self-assembly of novel porphyrin molecules wires, *Thin Solid Films* 499 (2006) 23–28.
- [44] J.M. Ribó, J. Crusats, J.-A. Farrera, M.L. Valero, Aggregation in water solutions of tetrasodium dipronated *meso*-tetrakis(4-sulfonatophenyl) porphyrin, *J. Chem. Soc., Chem. Commun.* (1994) 681–682.
- [45] S. Okada, H. Segawa, Substituent-control exciton in j-aggregates of protonated water-insoluble porphyrins, *J. Am. Chem. Soc.* 125 (2003) 2792–2796.
- [46] B.H. Schechtman, W.E. Spicer, Near infrared to vacuum ultraviolet absorption spectra and the optical constants of phthalocyanine and porphyrin films, *J. Mol. Spectrosc.* 33 (1970) 28–48.
- [47] P.B. Shea, A.R. Johnson, J. Kanicki, N. Ono, Electrical properties of staggered electrode polycrystalline tetrabenzoporphyrin organic field-effect transistors, *IEEE Trans. Electron Devices* 52 (2005) 1497–1503.
- [48] A. Bolognesi, M. Berliocchi, M. Manenti, A. Di Carlo, P. Lugli, K. Limouni, C. Dufour, Effects of grain boundaries, field-dependent mobility, and interface trap states on the electrical characteristics of pentacene TFT, *IEEE Trans. Electron Devices* 51 (12) (2004) 1997–2003.
- [49] A. Di Carlo, F. Piacenza, A. Bolognesi, B. Stadlober, H. Maresch, Influence of grain sizes on the mobility of organic thin-film transistors, *Appl. Phys. Lett.* 86 (26) (2005) 263501.
- [50] S.M. Sze, *Physics of Semiconductor Devices*, John Wiley & Sons, New York, 1981.
- [51] C. Clarisse, M. Riou, The operation and characteristics of diphthalocyanine field effect transistors, *J. Appl. Phys.* 69 (1991) 3324–3327.